Application of symmetric instability parameterization in the Coastal and Regional Ocean Community Model (CROCO)

Jihai Dong[1, 2], Baylor Fox-Kemper[3], Jinxuan Zhu[3] and Changming Dong[1, 2]

[1]School of Marine Sciences, Nanjing University of Information Science and Technology, Nanjing, Jiangsu, China.

[2]Southern Marine Science and Engineering Guangdong Laboratory (Zhuhai), Zhuhai, Guangdong, China.

[3]Department of Earth, Environmental, and Planetary Sciences, Brown University, Providence, Rhode Island, USA.

Corresponding author: Changming Dong (cmdong@nuist.edu.cn)

Key Points:

- A symmetric instabilitiy parameterization scheme is implemented in the CROCO
- The impacts of symmetric instability are evaluated based on three comparison simulations with different spatial resolutions
- The scheme captures the impacts of symmetric instability and improves the model simulation results

Abstract

As one kind of submesoscale instability, symmetric instability (SI) of the ocean surface mixed layer (SML) plays a significant role in modulating the SML energetics and material transport. The small spatial scales of SI, *O*(10 m ~ 1 km), are not resolved by current climate ocean models and most regional models. This paper describes comparisons in an idealized configuration of the SI parameterization scheme proposed by Bachman et al. (2017) (SI-parameterized) versus the K-Profile Parameterization (KPP) scheme (SI-neglected run) as compared to a SI-permitting model; all variants use the Coastal and Regional Ocean Community Model version of the Regional Ocean Modeling System (CROCO-ROMS) and this paper also serves to introduce the SI parameterization in that model. In both the SI-parameterized and SI-permitting model, the geostrophic shear production is enhanced and anticyclonic potential vorticity is reduced versus the SI-neglected model. A comprehensive comparison about the energetics (geostrophic shear production, vertical buoyancy flux), mixed layer thickness, potential vorticity, and tracer redistribution indicates that all these variables in the SI-parameterized case have structures closer to the SI-permitting case in contrast to the SI-neglected one, demonstrating that the SI scheme has a positive improvement to capture the impacts of SI. This work builds toward applying the SI scheme in a regional or climate model.

Plain Language Summary

Symmetric instability (SI) of the ocean surface mixed layer has spatial scales of tens of meters to kilometers, playing a significant role in ocean energy transfer and material transport. The coarse resolution of current climate and regional models cannot resolve SI due to its small scales, so its impacts require to be parameterized. This work impliments a SI parameterization scheme in the Coastal and Regional Ocean Community Model (CROCO) and the evalution indicates that the scheme improves the simulation results to capture the SI impacts. The work suggests a potential application of the sheme in a reginoal or climate model.

1 Introduction

Physical processes in the ocean surface mixed layer (SML) modulate the SML, impacting the energy budget of global ocean and thereby climate change. With spatial scales far from being resolved by climate ocean models (from tens of meters to kilometers), parameterizations of SML processes including surface waves, Langmuir circulation and submesoscale currents are a key avenue to improve climate and weather models (e.g., Fox-Kemper et al., 2008; Fox-Kemper et al., 2011; Noh et al., 2016; Qiao et al., 2016; Li et al., 2016). Among these processes, submesoscale instabilities can enhance vertical transports (e.g., Boccaletti et al., 2007; Lévy et al., 2012; Su et al., 2018), and energy cascades (e.g., Capet et al., 2008a; Buckingham et al., 2019; Dong et al., 2020a), which are dynamics requiring parameterization in ocean models.

The submesoscale consists of those processes with Rossby and Richardson numbers around *O*(1) (i.e., Ro ~ 1, Ri ~ 1) imparting time scales of hours to O(1) day and lengths of tens of meters to O(10) km (Thomas et al., 2008; McWilliams, 2016). Observations and simulations find submesoscales are ubiquitous over the globe (Callies et al., 2015; Buckingham et al., 2016; Su et al., 2018) and vertically over full water depth (Molemaker et al., 2015; Gula et al., 2016; Siegelman et al., 2019; de Marez et al., 2020). The SML is the layer of greatest submesoscale activity. Symmetric instability (SI) is a classical submesoscale instability, in that it requires rotation and some density variation, and it partially accounts for the SML submesoscale activity

(D'Asaro et al., 2011; Thomas et al., 2013; Thompson et al., 2016; Buckingham et al., 2019; Yu et al., 2019; Wenegrat et al., 2020).

In the SML, the Ertel potential vorticity (PV),

$$q = (f\mathbf{k} + \boldsymbol{\nabla} \times \mathbf{v}) \cdot \boldsymbol{\nabla} b, \tag{1}$$

is easily shifted toward anticyclonic values (i.e., opposite sign to local Coriolis parameter, *f*) at fronts through weak vertical stratification and strong horizontal buoyancy gradients. Here, $\boldsymbol{\nabla} = \frac{\partial}{\partial x}\mathbf{i} + \frac{\partial}{\partial y}\mathbf{j} + \frac{\partial}{\partial z}\mathbf{k}$ is the three-dimensional gradient operator, $\mathbf{v}$ is the three-dimensional velocity field, and $b = -g\rho/\rho_0$ is the buoyancy (g = 9.8 m s^{-2} is the gravitational acceleration, $\rho_0 = 1024$ kg m^{-3} is the background seawater density). Anticyclonic PV favors SI which is characterized by perturbation modes aligned along slanting isopycnals that feed on geostrophic shear of fronts (Stone, 1966; Hoskins, 1974; Haine & Marshall, 1998; Haney et al., 2015). The kinetic energy extracted by SI is transferred toward smaller scales and finally supports local mixing enhancement in the SML (Taylor & Ferrari, 2010; D'Asaro et al., 2011; Buckingham et al., 2019; Yu et al., 2019). SI also tends to restratify the SML, modulate the SML thickness, and redistribute passive tracers (Bachman et al., 2017; hereinafter B17). Given that fronts usually act as dynamical barriers to cross-front material transport, SI may be a significant routine for lateral exchange across fronts (Wenegrat et al., 2020).

The fastest growing wavelength of SI in the SML with a uniform stratification *N* and shear *U*/*H* (*U* is the velocity difference over the thickness of SI layer, *H*) can be estimated through linear instability analysis as (Stone, 1966)

$$L_{SI} = \frac{U}{f}\sqrt{1 - Ri_b}. \tag{2}$$

Here, $Ri_b = \frac{N^2 f^2}{|\boldsymbol{\nabla}_h b|^2}$ is the balanced Richardson number. In previous work, the authors (Dong et al. 2020b) use this relation to show that SI is expected to have spatial scales of O(10) m to O(1) km over the global ocean, thus all current climate models and even submesoscale-permitting regional models with resolutions of O(1) km are unable to directly resolve SI in most regions and seasons. The results from Dong et al. (2020b) also indicate that SI is active in the SML globally (in as much as 16% of wintertime regions) and potentially modulates the air-sea heat and momentum exchanges (reducing the usable wind-work reduction by 11% globally). As a result, the parameterization of SI in ocean models is expected to have a significant impact on simulation accuracy and prediction capability.

The goal of this work is to implement the SI parameterization scheme proposed by B17 in the Coastal and Regional Ocean Community Model (CROCO) and evaluate the simulation changes in terms of energetics, mixed layer thickness, potential vorticity and tracer redistribution based on an idealized configuration of two fronts under surface forcing. The rest of the paper is organized as follows: Section 2 introduces the theory of the SI parameterization and describes the model setup; Section 3 assesses the SI scheme based on three comparison cases. The last section discusses and concludes.

2 Symmetric instability parameterization and model setup

2.1 Symmetric instability parameterization

This section gives a brief description of the parameterization scheme that proposed by B17, although interested readers are referred to the greater detail of B17.

As SI can occur only when PV is anticyclonic, the SI layer, *H* is calculated as the depth below which fq_{bulk} becomes positive, which limits the deepest penetration depth of the unstable SI modes (Haney et al., 2015; Dong et al., 2020b),

$$fq_{bulk} = f\left(f\Delta b + \langle\zeta\rangle\Delta b + \Delta u\,\langle\frac{\partial b}{\partial y}\rangle - \Delta v\,\langle\frac{\partial b}{\partial x}\rangle\right) > 0. \quad (3)$$

Here, ζ is the vertical relative vorticity, Δ denotes the difference between the surface value and the value at a given depth, the angle bracket denotes a depth average over the same depth range. For a high-resolution model (such as the model used here), the vertical vorticity tends to be comparable to the local planetary vorticity, so we include the impacts of the vertical vorticity as suggested by Dong et al. (2020b) unlike the suggestion of B17.

As SI tend to mix and homogenize PV from the cyclonic values found in the stratified deeper layers into the anticyclonic region, surface forcing tending toward anticyclonic PV is necessary for sustained SI, called *forced* SI. The surface forcing driving anticyclonic PV injection (Thomas, 2005) includes sea surface heat and freshwater exchanges combined into the buoyancy forcing,

$$B_0 = B_T + B_S = g\alpha\frac{Q_{net\_heat}}{\rho_0 C_P} + g\beta(EP)S \quad (4)$$

and the Ekman Buoyancy Flux driven by along-front wind at the surface,

$$EBF = \frac{\boldsymbol{\tau}_w \times \mathbf{k}}{\rho_0 f}\boldsymbol{\nabla}_h b. \quad (5)$$

Here, α is the thermal expansion coefficient, Q_{net_heat} is the net surface heat flux, Cp = 4200 J kg^{-1} ^{o}C^{-1} is the seawater specific heat capacity, β is the saline contraction coefficient, *EP* is the net freshwater exchange due to evaporation and precipitation (the convection is for ocean loss of heat with positive Q_{net_heat} or freshwater with positive *EP*), and *S* is the sea surface salinity, and $\boldsymbol{\tau}_w$ is the wind stress. PV tends to be shifted toward anticyclonic values when $B_0 + EBF > 0$, i.e., toward convective destabilization. SI under $B_0 > 0$ and $EBF > 0$ have been studied using the Large Eddy Simulation (LES; e.g., Taylor & Ferrari, 2010; Thomas et al., 2013; Haney et al., 2015). The parameterization scheme proposed B17 relies heavily on forced SI for the rates of SI effects, combined with a condition that PV must be anticyclonic in order for the parameterization to be triggered.

The LES shows two distinct sublayers over the SI layer under $B_0 > 0$ and $EBF > 0$: a convective layer near the surface and a deeper SI-dominated layer below (e.g., Taylor & Ferrari, 2010). The relationship between the convective layer thickness, *h*, and the SI-layer, *H*, can be determined by a quartic equation (Thomas et al., 2013),

$$\left(\frac{h}{H}\right)^4 - c^3\left(1-\frac{h}{H}\right)^3\left[\frac{w_*^3}{U^3} + \frac{u_*^2}{U^2}cos\theta_w\right]^2 = 0. \quad (6)$$

Here, $c = 14$ is an empirical constant, $w_* = (B_0 H)^{1/3}$ is the convective velocity by surface buoyancy loss, $u_* = (|\boldsymbol{\tau}_w|/\rho_0)^{1/2}$ is the friction velocity, and θ_w is the angle between wind vector and frontal current.

Once *H* and *h* are known, the geostrophic shear production (GSP) describing the kinetic energy conversion rate to SI is parameterized as a piecewise linear function (Thomas et al., 2013),

$$GSP = \begin{cases} 0 & ,z = 0 \\ F_{SI}\frac{z+H}{H} - B_0\frac{z+h}{h} & ,-h < z < 0 \\ F_{SI}\frac{z+H}{H} & ,-H < z < -h \\ 0 & ,z < -H \end{cases}, \tag{7}$$

where $F_{SI} = EBF + B_0$ (see further discussion in B17). A corresponding SI vertical viscosity related to this kinetic energy extraction is calculated as,

$$\nu_{SI} = \frac{f^2}{|\nabla_h b|} GSP. \tag{8}$$

Assuming mixing takes on a simple form of the turbulent Prandtl number (i.e., $Pr = \frac{\nu_{SI}}{\kappa_{SI}}$), the vertical diffusivity is calculated by

$$\kappa_{SI} = \frac{2\nu_{SI}}{1+(10\max(0, Ri_b))^{0.8}}. \tag{9}$$

As mentioned in the preceding section, the overturning cells of SI can redistribute passive tracers isopycnally. This flux is accomplished by an along-isopycnal scalar diffusivity,

$$K_{SI} = \frac{GSP}{f^2}\min(1, {Ri_b}^2). \tag{10}$$

This along-isopycnal diffusivity is represented by a symmetric tensor in Redi (1982) form in the *z*-coordinate, which can be written as,

$$\mathbf{K}_{SI} = \frac{K_{SI}}{b_x^2+b_y^2+b_z^2}\begin{bmatrix} b_y^2+b_z^2 & -b_x b_y & -b_x b_z \\ -b_x b_y & b_x^2+b_z^2 & -b_y b_z \\ -b_x b_z & -b_y b_z & b_x^2+b_y^2 \end{bmatrix}. \tag{11}$$

In the CROCO, this along-isopycnal mixing is easily added via the built-in lateral tracer mixing along isopycnal surface algorithms.

As recommended by B17, the SI parameterization should be implemented alongside another default boundary layer turbulence closure, such as the nonlocal K-Profile Parameterization (KPP; Large et al., 1994) scheme used here, so that when the SI conditions are not met and SI is stable the other scheme is used. In practice, this means that the SI scheme is active only within frontal regions under destabilizing surface forcing. As the default turbulence scheme calculates momentum and tracer fluxes related to mixing, the SI scheme will be activated only when $B_0 > 0$ and $EBF > 0$ and h<0.95H (a convenient threshold value for SI activity, otherwise SI is dominated by convection). When the SI scheme is activated, the vertical fluxes, F_{wC} for tracers with nonzero surface fluxes in the convective layer needs to be considered, which can be parameterized as a linear profile,

$$F_{wC} = \begin{cases} 0 & ,z = 0 \\ F_0 \frac{z+h}{h} & ,-h < z < 0. \\ 0 & ,z < -h \end{cases} \quad (12)$$

Here, F_0 is the surface flux for a given tracer, C. We note that in both (7) and (12), the surface flux boundary condition is set to zero—this choice is necessary to ensure conservation of properties exchanged between the atmosphere and ocean: the SI scheme is designed to affect distributions within the SML, not the air-sea fluxes (although we will revisit this in the context of the SI-permitting runs later).

Finally, the momentum and tracer equations that include all these SI terms in the *z*-coordinate can be rewritten as,

$$\begin{cases} \frac{\partial u}{\partial t} + \boldsymbol{\nabla} \cdot (\mathbf{v}u) - fv = -\frac{\partial \phi}{\partial x} + \frac{\partial}{\partial z} \nu_{SI} \frac{\partial u}{\partial z} + \mathcal{F}_u + \mathcal{D}_u \\ \frac{\partial v}{\partial t} + \boldsymbol{\nabla} \cdot (\mathbf{v}v) + fu = -\frac{\partial \phi}{\partial y} + \frac{\partial}{\partial z} \nu_{SI} \frac{\partial v}{\partial z} + \mathcal{F}_v + \mathcal{D}_v \\ \frac{\partial C}{\partial t} + \boldsymbol{\nabla} \cdot (\mathbf{v}C) = \frac{\partial}{\partial z} \nu_{SI} \frac{\partial u}{\partial z} + \nabla \cdot (\mathbf{K}_{SI} C) - \frac{\partial F_{wC}}{\partial z} + \mathcal{F}_C + \mathcal{D}_C \end{cases} . \quad (13)$$

Here, $\boldsymbol{\nabla} = \frac{\partial}{\partial x}\mathbf{i} + \frac{\partial}{\partial y}\mathbf{j} + \frac{\partial}{\partial z}\mathbf{k}$ is the three-dimensional gradient operator, $\mathbf{v}$ is the three-dimensional velocity field, ϕ is the pressure potential, $\mathcal{F}$ and $\mathcal{D}$ are the corresponding forcing and horizontal diffusive terms, respectively. In this work, we will apply the SI scheme alongside the KPP as recommended by B17.

Steps to apply SI scheme in the CROCO are summarized as follows:

1) the momentum and tracer fluxes are calculated by the KPP;

2) then the surface bulk PV, q_{bulk} is calculated from the model fields and Equation (3), and the surface buoyancy flux, B_0, and the surface Ekman buoyancy flux, EBF are calculated from the surface fluxes in Equation (4−5);

3) For those grid points with $fq_{bulk} < 0$, $B_0 > 0$ and $EBF > 0$, the SI layer H is calculated based on Equation (3) and then the convective layer h can be determined by Equation (6);

4) If $\frac{h}{H} < 0.95$, the SI scheme is activated, and momentum and tracer fluxes are calculated to replace the values from the KPP using Equation (7−13). The CROCO uses the terrain-following coordinate (i.e., sigma-coordinate) system and details of introducing the sigma-coordinate and grid discretization can be referred to Chapter 3−4 of Hedström (2009).

2.2 Model setup

The parameterization and simulation are built with the CROCO (http://www.croco-ocean.org). The CROCO is a new model built upon the ROMS-Agrif (Jullien et al., 2019). The simulation in this work is still accomplished under the hydrostatic approximation.

An idealized model is established with a domain of 65 km × 65 km × 150 m (Figure 1). There are 60 layers in the vertical with finer resolution concentrated in the SML. The background state of the model has a constant salinity S = 35 PSU, and a vertical potential temperature profile as follows,

$$\theta(℃) = \begin{cases} 20 & ,-50 \le z \le 0 \\ 20 + 0.02(z+50), & -150 < z < -50 \end{cases}. \quad (14)$$

This profile provides a SML above 50 m and a thermocline below (Figure 1b). This linear thermocline profile yields a buoyancy frequency in the stratified interior of 75f. Based on the background temperature profile, two y-direction fronts in the SML with a horizontal scale of 3 km and a temperature difference of 0.3 ^{o}C are initialized at the beginning, yielding horizontal buoyancy gradients of 5.3f. A constant Coriolis parameter equivalent to a latitude of 35^{o} is chosen (f=8.4$\times 10^{-5}$ s^{-1}). Given the mixed layer depth of 50 m, this temperature difference and horizontal scale roughly match the mixed layer depth dynamically expected after geostrophic adjustment, i.e., the fronts are roughly one deformation radius wide when the boundary layer stratification is 28f. Meanwhile, a constant northward wind stress, τ = 0.03 N m^{-2} and a surface net heat flux with a diurnal cycle, $Q = 20\sin(2\pi T)$ W m^{-2} (T starts from 0 in days) are applied in the simulation. The heat flux here is much weaker (about one order of magnitude smaller) compared with the realistic one, chosen to favor a thick SI-dominated layer. In direction, the wind is in a downfront direction for the left front with a northward geostrophic current in Figure 1 (hereinafter NFront) and thus destabilizing but upfront for the right front with a southward geostrophic current (hereinafter SFront) and thus restratifying. A comparison between the two fronts will highlight frontal instabilities due to the downfront wind and EBF. The horizontal viscosity is chosen as 5 m s^{-2}. Periodic boundary conditions are used in the simulation. The simulation lasts for 20 days. Details about the model configurations are listed in Table 1.

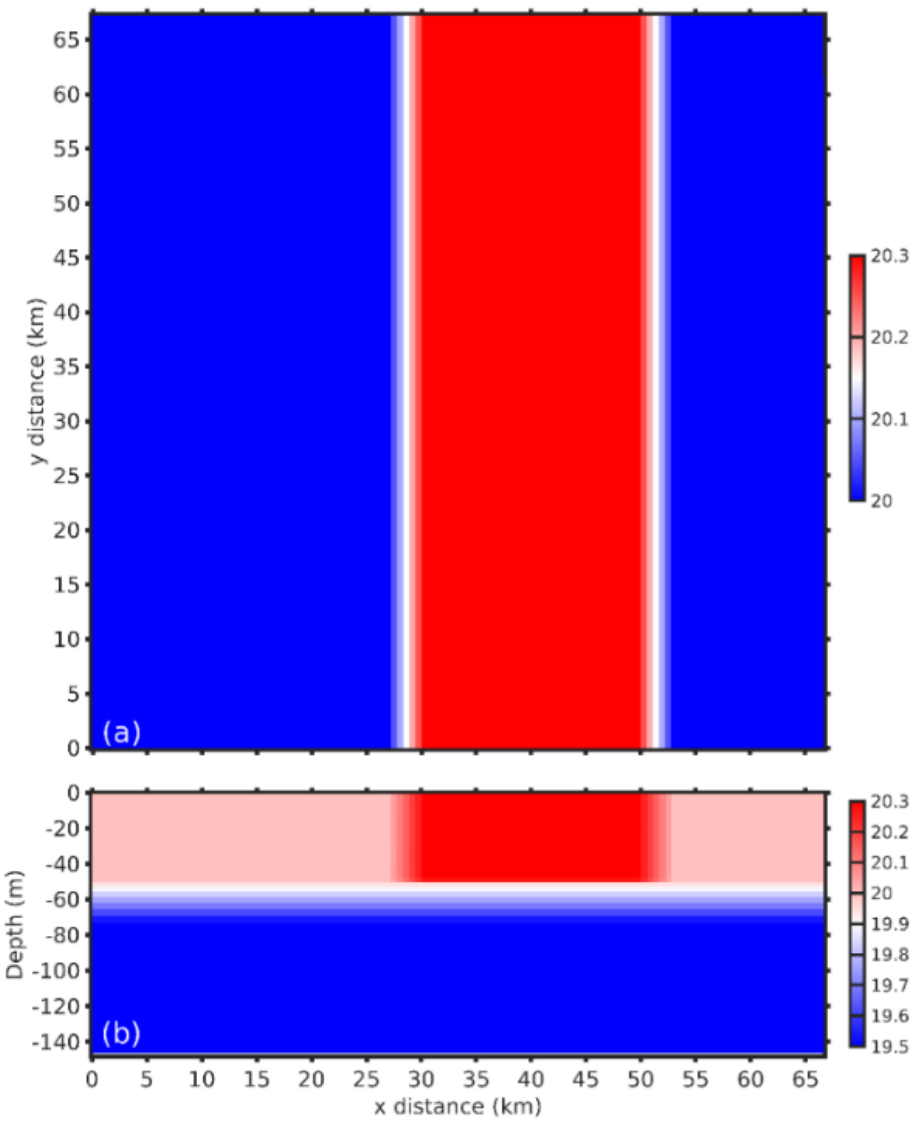

Figure 1 Potential temperature fields (^{o}C) in (a) the horizontal plane at the surface and (b) transverse plane in x direction.

Based on Equation (2), SI tends to have spatial scales about 0.5 ~ 1.5 km at the fronts during geostrophic adjustment with $0.25 \leq Ri_b \leq 0.95$. As a result, three comparison cases are conducted:

(1) **KPP550**: this case has a coarse spatial resolution of 550 m and the vertical mixing is accomplished solely by the KPP scheme;

(2) **SI550**: this case has a coarse spatial resolution of 550 m and the SI scheme is activated alongside the default KPP scheme;

(3) **KPP55**: this case has a high spatial resolution of 55 m with the KPP scheme, which is intended to resolve SI directly (partially resolved, see the discussion section). According to Bachman & Taylor (2014), the impacts of SI are only partially accomplished in a model that

partially resolves SI due to coarse resolution or large horizontal viscosity, yielding qualitative but not quantitative agreement. A discussion of the potential impacts from resolution limitations and the hydrostatic approximation follows the results.

Table 1 Model configurations of the different cases.

Parameter	Case		
	KPP550	SI550	KPP55
Domain size	65 km × 65 km × 150 m	65 km × 65 km × 150 m	65 km × 65 km × 150 m
Horizontal Resolution	550 m	550 m	55 m
Vertical layers	60	60	60
Initial SML depth	50 m	50 m	50 m
Front scale	3 km	3 km	3 km
Temperature difference	0.3 ^{o}C	0.3 ^{o}C	0.3 ^{o}C
Horizontal buoyancy gradient	5.3f	5.3f	5.3f
Thermocline stratification	75f	75f	75f
Surface wind stress	0.03 N m^{-2}	0.03 N m^{-2}	0.03 N m^{-2}
Heat flux	20 W m^{-2}	20 W m^{-2}	20 W m^{-2}
Coriolis parameter	8.4×10^{-5} s^{-1}	8.4×10^{-5} s^{-1}	8.4×10^{-5} s^{-1}
Horizontal viscosity	5 m s^{-2}	5 m s^{-2}	5 m s^{-2}
Turbulence scheme	KPP	SI+KPP	KPP

A similar two-front setup has been used to investigate submesoscale instabilities, including interactions with Langmuir turbulence (Hamlington et al., 2014), impacts on tracer transports (Smith et al., 2016), and the application of the SI scheme in the MIT general circulation model (Zhu, 2017). As the fronts evolve, different frontal instabilities occur and two notable instabilities are mixed layer instabilities (MLI; Boccaletti et al., 2007; Fox-Kemper et al., 2008) and SI (Hoskins, 1974; Taylor & Ferrari, 2010; Thomas et al., 2013; B17), which are the typical submesoscale instabilities that occur along fronts in the absence of strain (Haine & Marshall, 1998; Haney et al., 2015). The spatial resolution of the coarse-resolution cases can resolve MLI but hardly SI, while the resolution of the high-resolution case is supposed to resolve both MLI and SI. Neither resolution resolves convective boundary layer turbulence, nor would this be accurately modeled in a hydrostatic system, so even in the high-resolution simulation the KPP is used.

3 Results

3.1 Symmetric instability in KPP55 and primary comparison

Acting as a "truth" case, the SI-resolving or SI-permitting degree of the high-resolution case (i.e., KPP55) needs to be clarified (Bachman & Taylor, 2014). To compare this high-resolution run against the coarser runs, a highpass filter with a cutoff scale of 1 km is applied on the velocity fields in KPP55. The chosen cutoff scale is near the Nyquist sampling rate of the coarse-resolution cases, indicating that the velocity perturbations retained after the filter is applied are not resolved by the coarse-resolution cases (i.e., KPP550 and SI550). The instantaneous transverse sections of PV and the cross-front (i.e., x-direction) velocity perturbations are investigated (Figure 2; Figure 3; Figure 4). The surface net heat flux at 9.25 days is negative and thus heats the ocean, leading to vertical restratification and positive PV for most regions (Figure 2a). Weak negative PV values can still be observed between 20 ~ 50 m, a residual of the previous nighttime cooling. The only exception is at the location of the EBF-destabilized front (i.e., NFront), where strong negative PV values occupy the whole SML as a result of the strong horizontal buoyancy gradients and vertical shear (Equation (2-3)). The SI layer thickness calculated based on the bulk PV is negligible everywhere but quite thick at the frontal regions where this negative PV is present (yellow line in Figure 2a). Precisely occupying the region of negative PV, remarkable alternating cross-front velocity perturbations typical of SI concentrating around the NFront with magnitude up to 0.02 cm s^{-1} are observed (Figure 2b, Figure 4c).

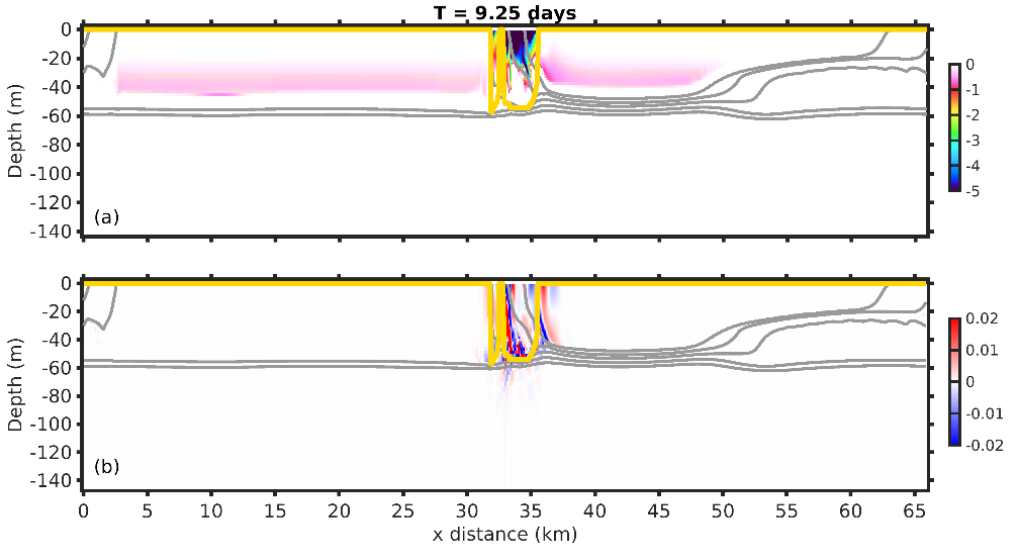

Figure 2 Transverse sections of the instantaneous (a) PV ($\times 10^{-10}$ s^{-3}) and (b) cross-front velocity perturbations (cm s^{-1}) at 9.25 days. The gray lines denote isolines of potential density, and the yellow lines denote the SI layer thickness determined by Equation (3).

At 9.75 days, the net surface heat flux is positive (ocean cooling) with the maximum magnitude, eroding the stratification and injecting negative PV. As a result, PV becomes negative in the SML over most regions, except near the SFront where strong EBF-driven

stratification due to isopycnals is subject to Ekman overturning and flattening (Figure 3a). Nevertheless, strong velocity perturbations are still observed only at NFront.

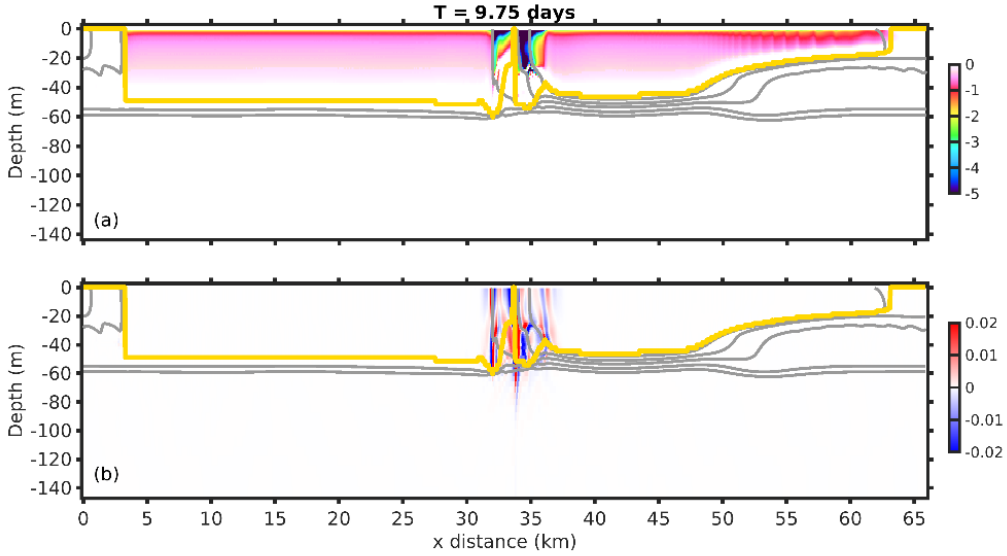

Figure 3 Transverse sections of the instantaneous (a) PV ($\times 10^{-10}$ s^{-3}) and (b) cross-front velocity perturbations (cm s^{-1}) at 9.75 days. The gray lines denote isolines of potential density, and the yellow lines denote the SI layer thickness from Equation (3).

Zooming in near the destabilized front indicates that the velocity perturbations are dominated by along-isopycnal modes and mainly concentrate at the frontal regions with negative PV (Figure 4): characteristics of SI (e.g., Bachman & Taylor, 2014; Haney et al., 2015). By 9.25 days, the region of SI activity is well characterized by the SI layer depth derived based on the bulk PV equation (Figure 4a, c). Although the SI layer is deepened by surface cooling, the SI modes at day 9.75 are still confined at the frontal region as a result of their extraction of geostrophic shear energy.

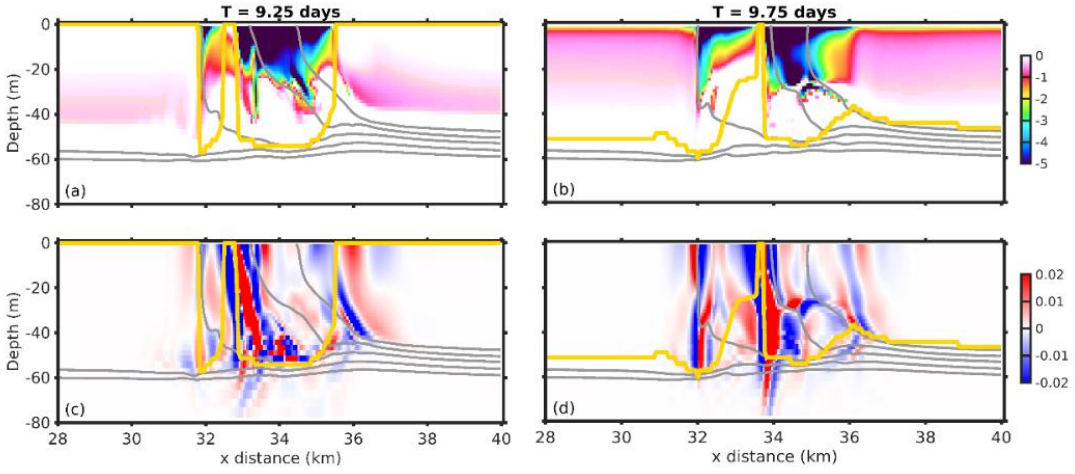

Figure 4 A zoom-in view on the transverse sections of (a, b) PV ($\times 10^{-10}$ s^{-3}) and (c, d) cross-front velocity perturbations (cm s^{-1}) at NFront. The gray lines denote isolines of potential density, and the yellow lines denote the SI layer thickness from Equation (3).

The three cases are first compared by examining the temperature and PV fields after 18 days—close to the end of simulation (Figure 5). The downfront wind strengthens the horizontal gradients at NFront, making it sharper and more unstable and MLI generates meanders and eddies, in contrast to SFront which is widened as it overturns (as seen in Hamlington et al. (2014)). Figure 5 shows that active meanders and eddies are observed at NFront in both surface temperature and PV from all three cases. The surface fluxes are warming the ocean at 18.25 days, so the surface PV is generally positive excepting the negative values at NFront. Despite the diverse instability structures at the surface among these cases, the transverse sections of the along-front averages reveal systematic differences reflecting SI impacts (Figure 6). The temperature sections are similar in the three cases, showing a shallow SFront and a deep NFront. The PV is similar at SFront but quite different at the three simulations' NFront. One expects MLI at NFront to lead to potential energy release and mixed layer restratification (Boccaletti et al., 2007). Thus, at NFront the mixed layer depth is shoaled by MLI and positive PV intrudes to shallow depth above 20 m in all three simulations. However, compared with KPP550, the positive PV intrudes to a shallower depth in SI550 and KPP55 (Figure 6d, e, f), a result of the SI transport of stratified water into the mixed layer. Correspondingly, the KPP boundary layer depths, H_{KPP} determined by a critical bulk Richardson number of 0.3 (Large et al., 1994) is shallower at the fronts in the SI550 and KPP55 cases (gray lines in Figure 6d, e, f).

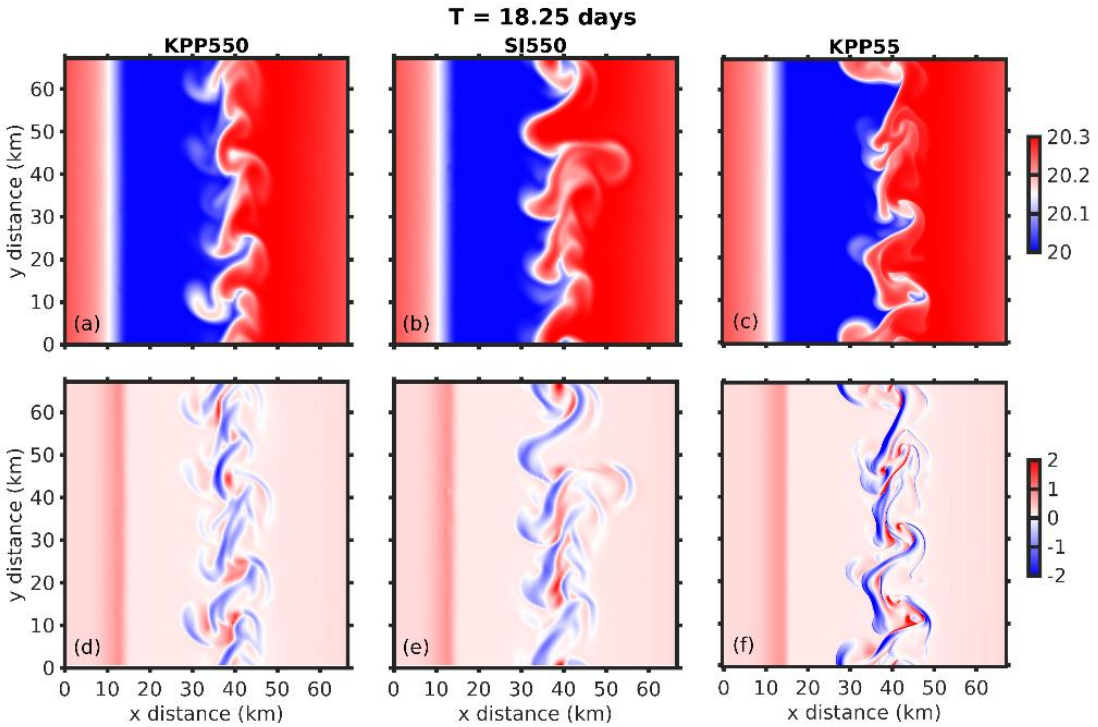

Figure 5 Surface distributions of the instantaneous (a, b, c) temperature (^{o}C) and (d, e, f) PV ($\times 10^{-9}$ s^{-3}) at 18.25 days. The left, middle and right columns are results from KPP550, SI550 and KPP55, respectively.

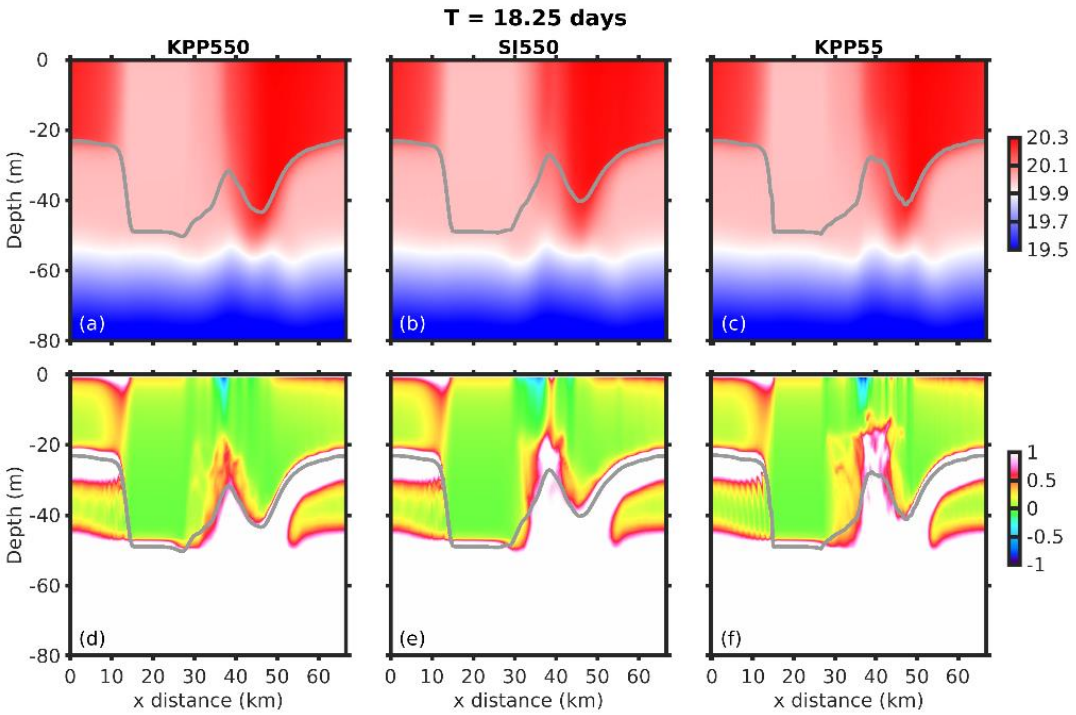

Figure 6 Transverse sections of the y-direction averaged (a, b, c) temperature (^{o}C) and (d, e ,f) PV ($\times 10^{-9}$ s^{-3}) at 18.25 days. The gray lines denote the KPP boundary layer depth. The left, middle and right columns are results from KPP550, SI550 and KPP55, respectively.

At 18.75 days, the intensified surface cooling results in negative PV in the SML, but the strongest negative PV is still at NFront (Figure 7). B_0 and *EBF* are both cooling at the NFront at this time, and the derived SI layer depth *H* and convective layer depth *h* are shown (purple and black lines in Figure 8). These three depths (including H_{KPP}) overlap at most regions, but are distinct at NFront, consistent with the expectation of SI effects there in SI550 and the realization of SI effects in KPP55. The convective layer is shallower than the KPP boundary layer depths, while the SI layer is deeper (per B17).

Overall, when the SI parameterization is included, the KPP boundary layer and SI layer both become shallower due to the specified restratification by SI, which is closer to the high-resolution simulation result in KPP55, compared with the coarse-resolution case KPP550 which does not parameterize any restratification. SI dominates below the convective layer depth and the mechanism for restratification is SI-driven exchange of stratified thermocline water by SI between the SML and the deeper layers near *H* compared with the KPP550 result which has limited parameterized effect below H_{KPP}.

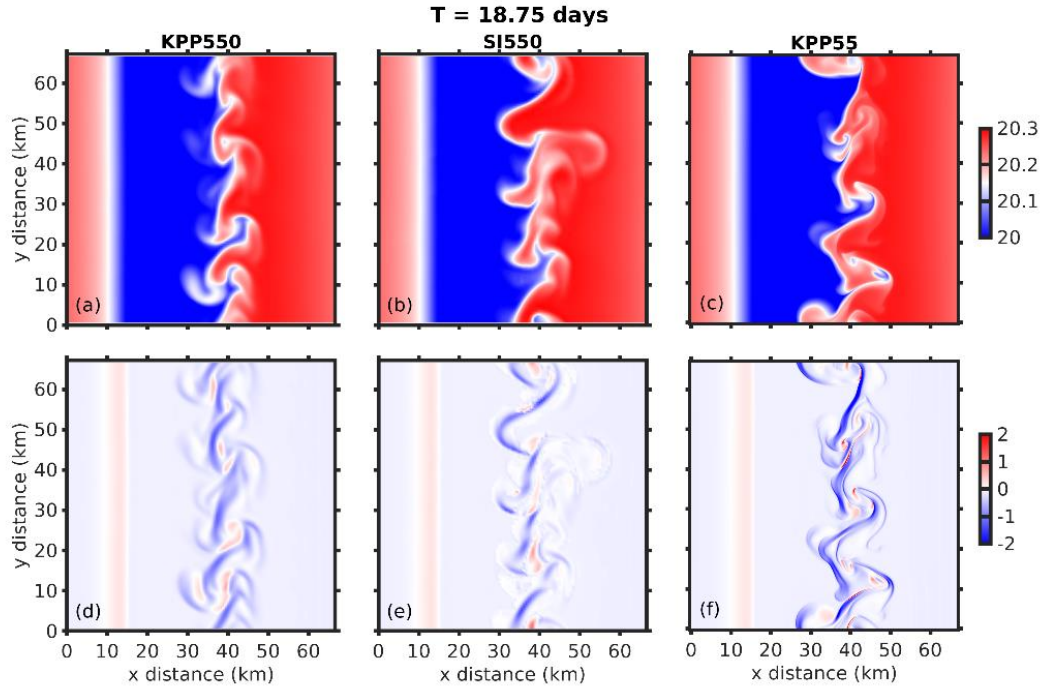

Figure 7 Surface distributions of the instantaneous (a, b, c) temperature (°C) and (d, e, f) PV ($\times 10^{-9}$ s^{-3}) at 18.75 days. The left, middle and right columns are results from KPP550, SI550 and KPP55, respectively.

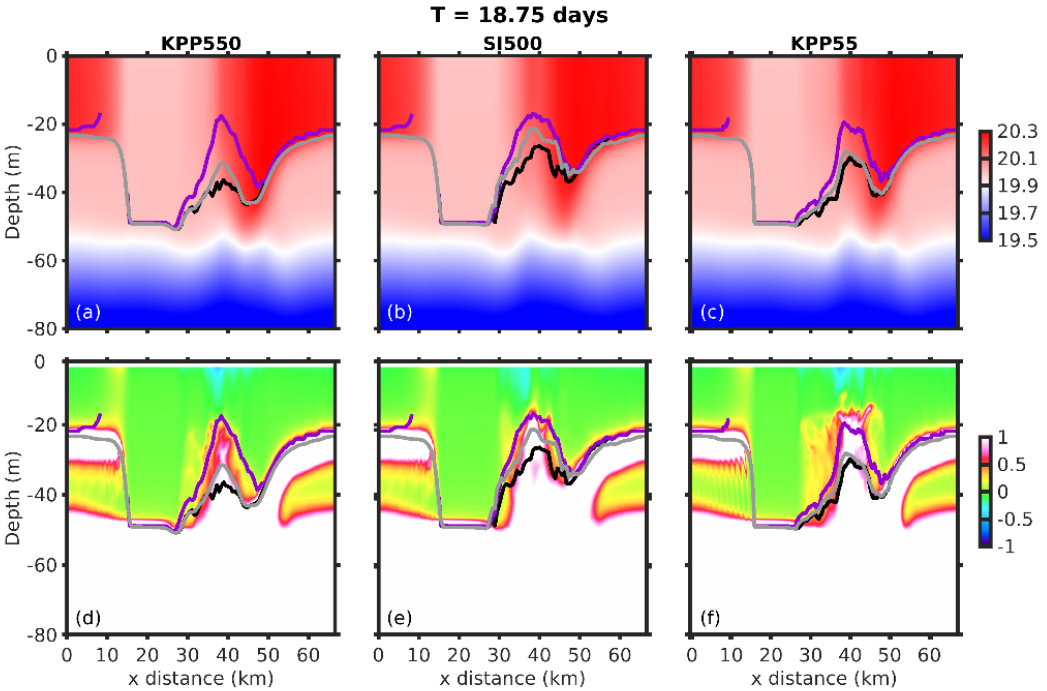

Figure 8 Transverse sections of the y-direction averaged (a, b, c) temperature (°C) and (d, e ,f) PV ($\times 10^{-9}$ s^{-3}) at 18.75 days. The purple, gray and black lines denote the convective layer depth (h), KPP boundary layer depth (H_{KPP}) and SI layer depth (H), respectively. The left, middle and right columns are results from KPP550, SI550 and KPP55, respectively.

347

348 3.2 Energetics

349 Fundamentally, energetics analysis is useful for assessing the effects of the SI
350 parameterization scheme, as SI grows by extracting the geostrophic kinetic energy of frontal
351 currents. To assess these three cases, the velocity, temperature and buoyancy fields are
352 decomposed into the background, MLI and SI components, namely,

353
$$\begin{cases} \mathbf{u} = \mathbf{u}_b + \mathbf{u}' = \mathbf{u}_b + \mathbf{u}_{MLI} + \mathbf{u}_{SI} \\ w = w_b + w' = w_b + w_{MLI} + w_{SI} \\ \theta = \theta_b + \theta' = \theta_b + \theta_{MLI} + \theta_{SI} \\ b = b_b + b' = b_b + b_{MLI} + b_{SI} \end{cases}. \quad (15)$$

354 Here, the background component is calculated by whole-domain averaging in the along-front
355 direction (i.e., y-direction), the SI component is calculated by a highpass filter with a cutoff scale
356 of 1 km (this scale is just below the scale that the coarse-resolution cases can resolve, so the SI
357 component is expected to be zero for those cases), and the MLI component is the residual after
358 removing these large and small scale components. The background horizontal velocity
359 component is further decomposed into the geostrophic and Ekman/ageostrophic components,
360 $\mathbf{u}_b = \mathbf{u}_g + \mathbf{u}_E$. The geostrophic component is determined based on the thermal wind balance
361 ($f\mathbf{k} \times \frac{\partial \mathbf{u}_g}{\partial z} = -\nabla_h b_b$; note there is only v_g and u_g should be zero based on this calculation).

362 Based on the decomposition, the GSP is calculated as (with overbar denoting horizontal
363 averages, and the whole equation is calculated as an integral over the horizontal),

364
$$GSP = K_v(\frac{\partial \mathbf{u}_g}{\partial z})^2 - \overline{\mathbf{u}'w'}\frac{\partial \mathbf{u}_g}{\partial z}, \quad (16)$$

365 where K_v is the model output vertical viscosity, noting that in the coarse-resolution simulations
366 this viscosity is intended to capture the full GSP by SI (B17). The vertical buoyancy flux is
367 evaluated in two contributions: the vertical buoyancy flux, BF related to vertical diffusivity and
368 SI (parameterized or resolved) and the vertical buoyancy production, BP, related to potential
369 energy release due to MLI. The BF is calculated as,

370
$$BF = -g\alpha K_t\left(\frac{\partial \theta_b}{\partial z} - \gamma_\theta\right) \quad (17)$$

371 in KPP550,

372
$$BF = -g\alpha K_t\left(\frac{\partial \theta_b}{\partial z} - \gamma_\theta\right) + w_{SI}b_{SI} \quad (18)$$

373 in KPP55 and

374
$$BF = -K_t N^2 + g\alpha F_{w\theta} \quad (19)$$

375 in SI550. Here, K_t is the model output vertical diffusivity, γ_θ is the nonlocal heat transport term
376 (Large et al., 1994), and $F_{w\theta}$ is the vertical heat convection determined by Equation (12) for the
377 parameterized SI tracer transport. Note that the along-isopycnal transport of buoyancy is zero, by
378 the rotated diffusion (Redi, 1982) formulation of Equation (11). The BP is calculated for the MLI
379 contribution as

380
$$BP = w_{MLI}b_{MLI} \quad (20)$$

in all the three cases.

The vertical profiles of the horizontally-averaged GSP, BF and BP calculated over NFront (considering the fronts moves from west to east, a x-direction 30-km range covering the front is chosen for averaging and the same below) during times of cooling (positive surface heat flux to trigger the SI parameterization) over simulation days 8 through 12 are shown in Figure 9. The calculated GSP in all three cases is nearly zero below the SML and positive in the SML, implying an extraction of energy from the frontal geostrophic shear (Figure 9a). However, the GSP profile in the coarse-resolution case KPP550 is relatively weak as it results only from the KPP vertical viscosity damping of the sheared front (blue line in Figure 9a). In contrast, the GSP in the SML in the high-resolution case KPP55 (red line in Figure 9a) is enhanced by about 2 ~ 3 times over KPP550. This GSP enhancement is attributed to the resolved SI in the high-resolution case that grows by extracting frontal kinetic energy and weakening the frontal geostrophic shear. The SI scheme is designed to mimic this behavior, and when activated in the coarse-resolution simulation SI550, the calculated GSP profile (green line in Figure 9a) is obviously improved and closer to the high-resolution case.

Under the SI-induced vertical buoyancy flux, the BF is also expected to be enhanced in the SML (Figure 9b). Figure 9b indeed shows the BF is negative and weak below the SML, consistently in the three cases. The weak negative BF is the signature of entrainment through vertical mixing (Grant & Belcher, 2009; Li & Fox-Kemper, 2017, 2020). In the SML, the BF becomes positive indicating restratification of the SML via both surface forcing and entrained fluid. Two processes may contribute to this restratification. One is the convection process near the surface. The surface cooling leads to surface buoyancy loss and weaker stratification in the SML, carried out by the vertical convection and upward buoyancy flux (dense water moving downward). The other process is SI. To restore PV to a neutral state (i.e., PV=0) and reach marginal SI stability, the overturning cells associated with SI tend to flatten the slanted isopycnals at fronts, leading to restratification (Bachman & Taylor, 2014; B17). In KPP550, the positive BF can only be caused by surface convection. However, as the resolution increases, the BF is enhanced especially at the lower SML in KPP55 with a notable increase of more than 60% near 25 m depth—indicative of the resolved SI restratification. The SI scheme is designed to mimic the enhanced BF and the SI550 simulation indeed becomes closer to the high-resolution BF result of KPP55. Compared with the high-resolution result, a similar parameterized increase of about 50% in the SI550 at about 25 m depth is observed. Given that the buoyancy flux forcing inducing convection is consistent between the three cases, the enhancement at the lower SML in the SI550 and KPP55 is cleanly attributable to SI restratification.

Unlike the GSP and BF, the BP associated with MLI is modestly weakened during simulation days 8 through 12 if the SI impacts are resolved or parameterized (Figure 9c). Generally, the BP is zero below the SML but positive in the SML, implying available potential energy release (e.g., Boccaletti et al., 2007; Fox-Kemper et al., 2008). This positive BP also indicates SML restratification by MLI, which should be the dominant or a significant factor for the SML shallowing in the coarse-resolution case KPP550 (Figure 6d and Figure 8d), as the SI impacts are not included in that simulation. In this case, the SI plus convective restratification BF exceeds the MLI restratification BP, but as the different effects scale very differently with frontal strength and surface forcing (Fox-Kemper et al., 2008; B17), this is not expected to be a general result.

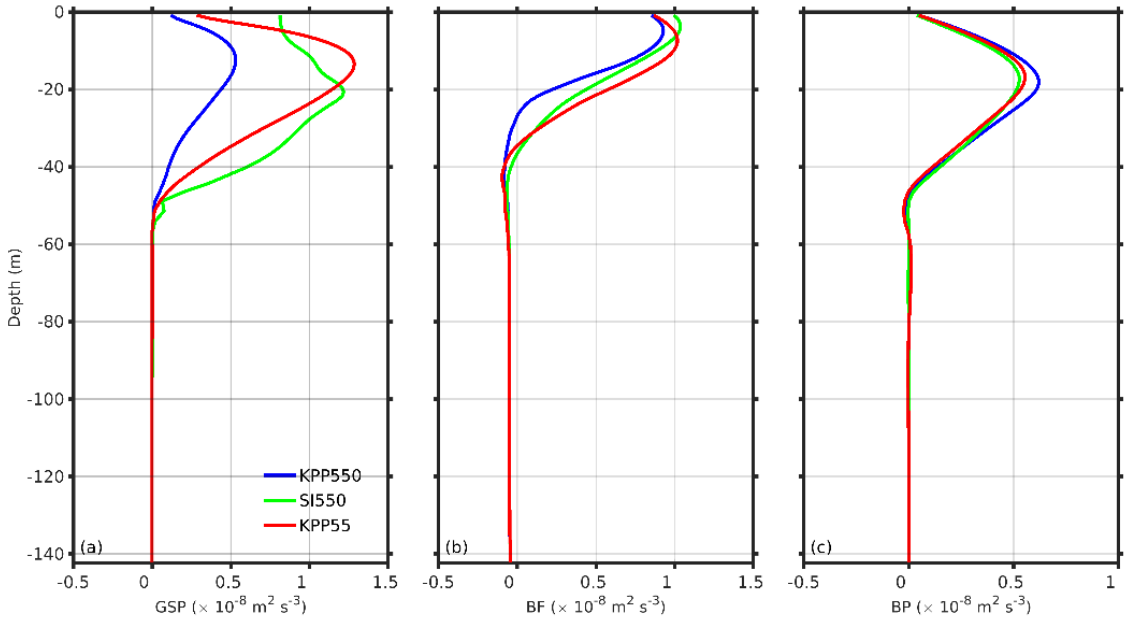

Figure 9 Vertical profiles of (a) geostrophic shear production, GSP ($m^2\ s^{-3}$), (b) vertical buoyancy flux, BF ($m^2\ s^{-3}$), and buoyancy production, BP ($m^2\ s^{-3}$) averaged over a 30km region enclosing NFront during cooling periods of simulation days 8 through 12.

The GSP, BF and BP capture the different kinetic and potential energy production due to SI among the three simulations. Rather than averaging over windows, the total time evolution of the kinetic energy and potential energy densities averaged over NFront are analyzed (Figure 10) which reveal directly the integrated effects of these distinct energy budgets among the models. In addition to diurnal and inertial oscillation variability, the kinetic energy of the along-front currents (i.e., in y-direction average) shows differences between three cases: the magnitudes in both SI550 and KPP55 are generally weaker than that in KPP550 after 10 days (Figure 10a), although the differences are modest in comparison to the oscillations present in all three runs. The enhanced GSP due to SI contributes to the differences. If the ageostrophic Ekman and inertial currents are removed, the kinetic energy of the geostrophic currents (diagnosed from the along-front averaged density fields) dominates the total along-front kinetic energy (Figure 10b). The relatively weaker kinetic energy is still observed in SI550 and KPP55.

One aspect of the energy cycle obscuring the SI effect is that the submesoscale kinetic energy related to MLI is also modulated by SI (Figure 10c), as suggested by the BP in Figure 9d. As MLI begin to grow (after 8 days), the submesoscale kinetic energy increase is slowed down in both SI550 and KPP55, compared with the result in KPP550 (Figure 10c). This evolution is consistent with the calculated BP profiles in Figure 9d, since the BP that fuels MLI is weakened when SI is resolved or parameterized, suppressing MLI. However, this situation is reversed after about 12 days. Then submesoscale kinetic energy becomes stronger in SI550 and KPP55, as more potential energy is converted into MLI. Apparently, BP is strengthened after 12 days (not shown). The potential energy over NFront decreases consistently during the simulation, and slightly lower energy content can be observed in SI550 and KPP55, especially after 15 days (Figure 10d), a difficult to anticipate result of both the enhanced mixing and enhanced

restratification in these runs. Note that even while the energetic consequences of SI are modest in comparison to other changes in these simulations, the effects on stratification and PV are not (see next section).

The energetic analysis here indicates that SI can not only decrease the frontal geostrophic shear, but also modulate the growth of MLI. The MLI kinetic energy evolution is firstly suppressed at the beginning and then enhanced due to the impacts of SI. The primary goal of this work is focused on the implementation and effects of the SI parameterization in the CROCO, and further analysis about the interactions between SI and MLI are not conducted here. Underlying mechanisms for the interactions need be clarified in the future, although it is perhaps telling—or coincidental—that the effect is common to both the resolved and parameterized SI.

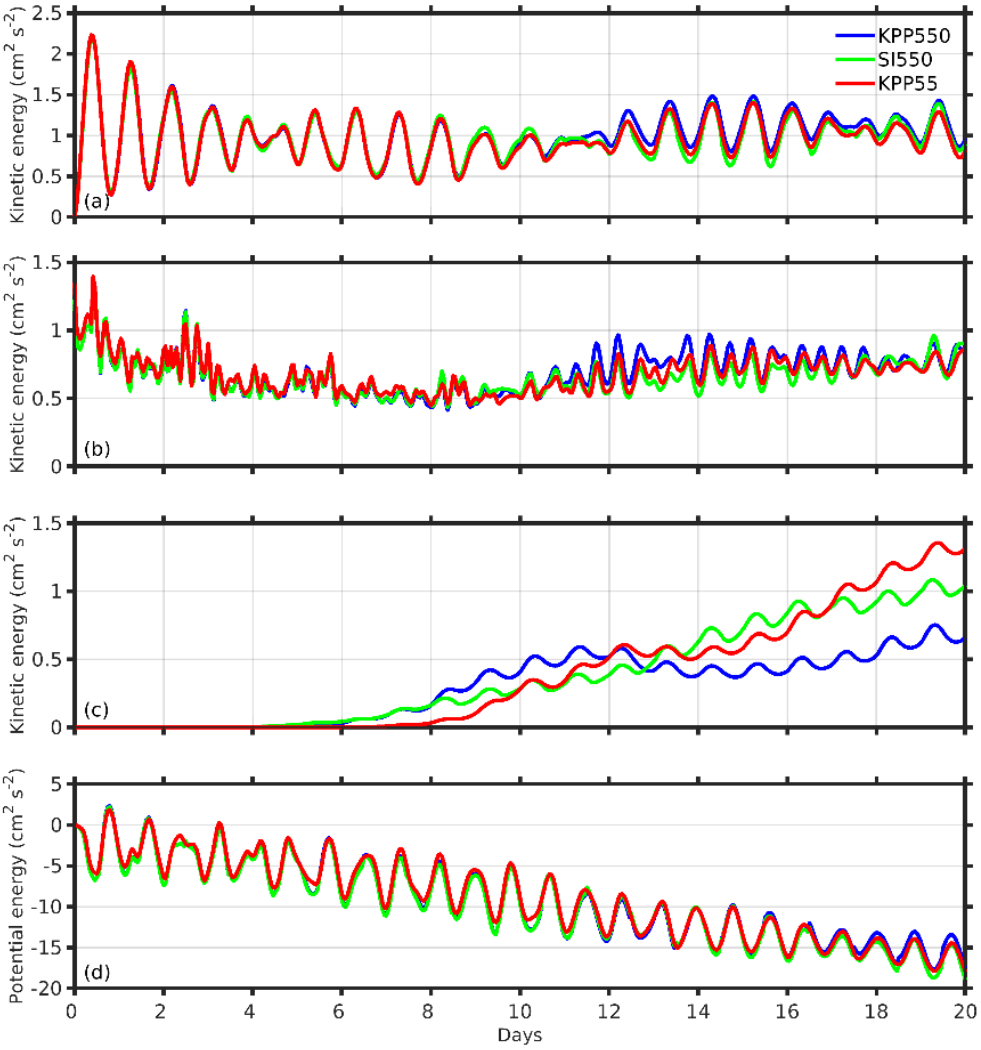

Figure 10 Time evolution of the (a) along-front kinetic energy density (cm^2 s^{-2}), (b) along-front geostrophic kinetic energy density (cm^2 s^{-2}), (c) MLI kinetic energy density (cm^2 s^{-2}) and (d) potential energy density (cm^2 s^{-2}) averaged on over NFront.

3.3 Mixed layer thickness and potential vorticity

The transverse sections of temperature and PV in Figure 6 and Figure 8 show the SML shoaling as SI is resolved or parameterized. Quantitative analysis of the mixed layer thickness changes is conducted in this section. Here, the mixed layer thickness is defined as the depth at which the surface potential density increases by a value of 0.03 kg m^{-3} (following de Boyer Montégut et al. (2004)). The mixed layer depth averaged over NFront has a shoaling trend over the simulation time (Figure 11a). The mixed layer thickness tends to vary in conjuction with MLI energy. Initially, the mixed layer thicknesses in the three cases covary in time. As MLI begins to grow after 8 days, the mixed layer thicknesses begin to differ. SI550 and KPP55 have slightly deeper mixed layers at this stage compared with the KPP550, but they grow shallower as time evolves. There is quantitative agreement in differences of the mixed layer thicknesses between SI550 and KPP550 (green line in Figure 11b) and KPP55 and KPP550 (red line in Figure 11b) over time. The difference is positive and less than 1 m between simulation days 8 and 10, but afterward becomes negative between 1 ~ 2 m. Compared with the overall mixed layer thickness, the SI effect accounts for a small fraction in these simulations. However, how much SI contributes to the mixed layer restratification depends on the SI activity and strength, so a realistic simulation is needed for quantitative assessment.

The mixed layer depth covaries with MLI kinetic energy, but this correlation may not be causal. The SML restratification is induced by SI as well in two ways: the upward buoyancy flux associated with MLI is modulated by SI, which shoals the SML, and SI tends to flatten isopycnals to reduce negative PV, leading to SML restratification. It is hard to distinguish these two SI and the perturbed MLI contributions here, but one can attribute the total changes to SI as parameterized or resolved.

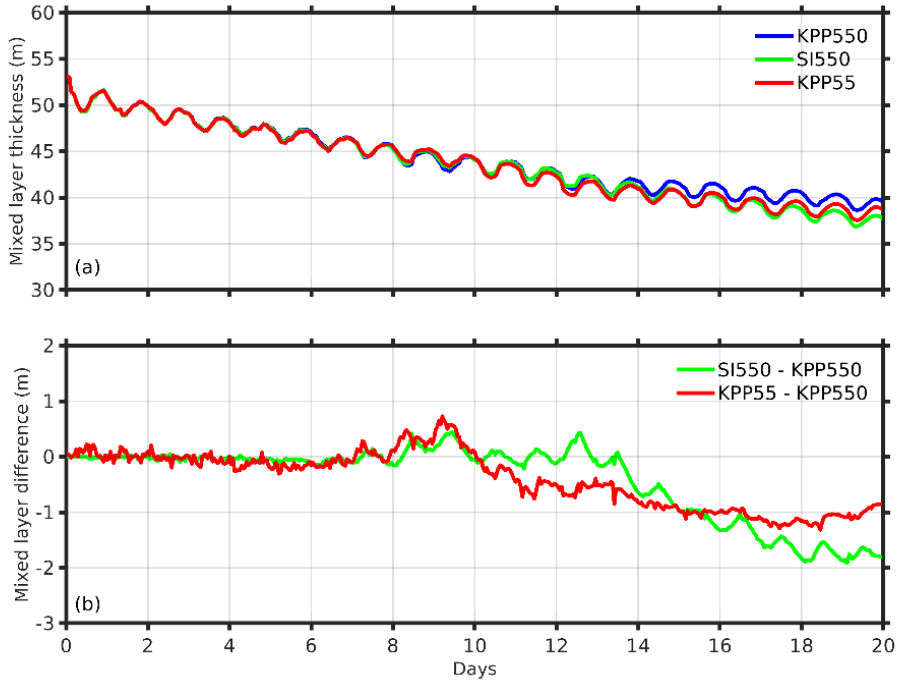

Figure 11 Time evolution of (a) mixed layer thickness (m) and (b) differences (m) averaged over NFront. The mixed layer thickness is determined with a threshold potential density value of 0.03 kg m^{-3} (de Boyer Montégut et al., 2004).

A direct impact from SI is the ability to reduce negative PV and restore PV to a neutral state. Different percentiles of PV in the upper 30 over NFront demonstrate this impact from SI (Figure 12). Due to the horizontal buoyancy gradients of the front, the median PV is negative in the three cases (Figure 12b). The median PV in both SI550 and KPP55 is closer to zero (neutral state) as expected, compared with KPP550, as SI is expected to bring up stratified thermocline waters to oppose surface forcing and approach marginal stability for SI—zero PV. Meanwhile, the reduction of negative PV also shifts the 10^{th} and 90^{th} percentiles, an indicator of the complex spatial variety of the SI-MLI combination illustrated in Figures 5 and 8. The 10^{th} percentile of PV in SI550 is shifted to a smaller negative value in contrast to KPP550 and KPP55 (Figure 12c). PV is scale-dependent, and the magnitude of surface forcing will become larger as grid spacings become finer (Bodner & Fox-Kemper, 2020). But the 10^{th} PV in KPP55 is comparable with the value in the KPP550 here. For the 90^{th} percentile of PV, it is positive and moves to larger values under the SI impact (Figure 12a), consistently among the resolved- and parameterized-SI cases.

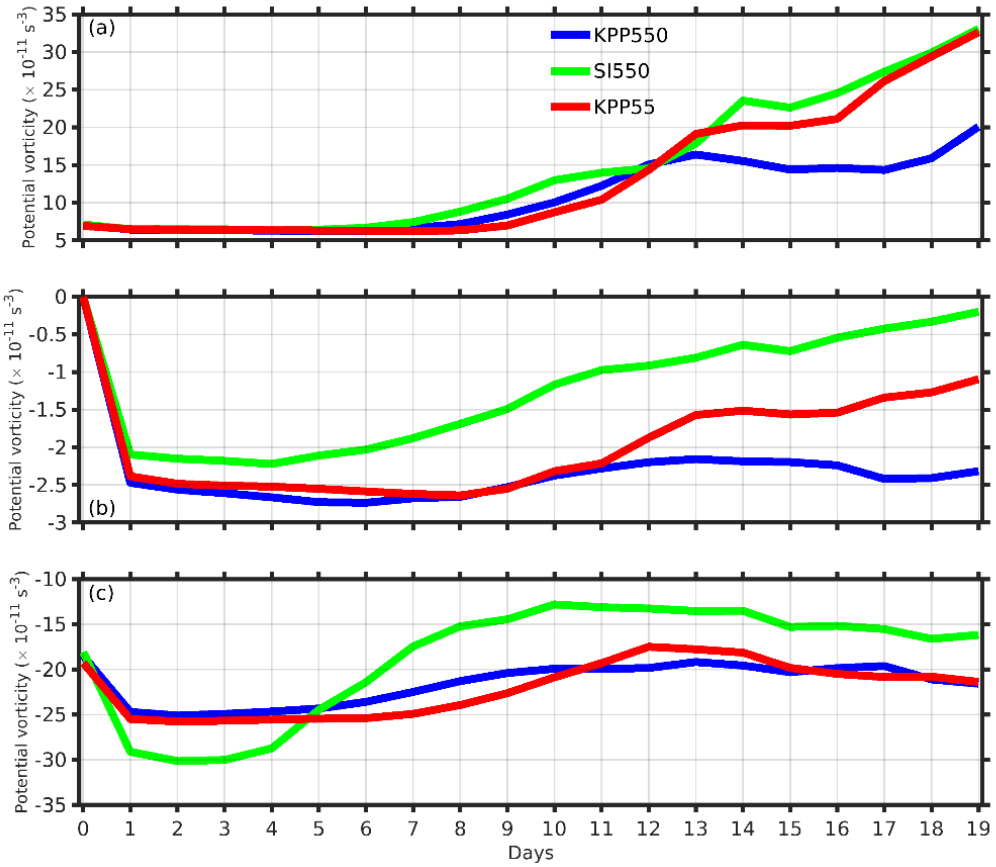

Figure 12 Time evolution of the (a) 90^{th} percentile, (b) median and (c) 10^{th} percentile values of PV (s^{-3}) in the upper 30 m over NFront.

The probability density functions (PDF) of PV in the upper 30 m (within the SML) at the last day in the three cases are calculated and shown in Figure 13. The PDF of PV is clearly

modulated by SI. A consistent elevated tail on the positive PV value side of the PDF occurs in both SI550 and KPP55 (Figure 13a). For negative PV values, the PDF tail in SI550 is depressed, while in contrast KPP55 is depressed only for weaker values (roughly PV≥-0.5×10^{-9} s^{-3}) and elevated for more negative PV. Large negative PV probability in KPP55 is significantly higher than either KPP550 or SI550, which may not be an effect of SI but rather an attribute of PV injection due to the finer grid spacings. The PDFs in all cases have positive skewnesses due to centrifugal instability (e.g., Capet et al., 2008b). Overall, SI changes the asymmetry of the PDF by elevating positive PV and decreasing negative PV (although surface forcing counters this effect). The calculated skewness of the PDF in KPP550 is 0.11, and increased to 0.16 and 0.15 in SI550 and KPP55, respectively. The PV reduction by SI is further highlighted if we integrate the PDFs over the negative PV range (Figure 13b). The probability of negative PV in KPP55 is 0.61, but decreases to 0.51 in SI550 and 0.54 in KPP55.

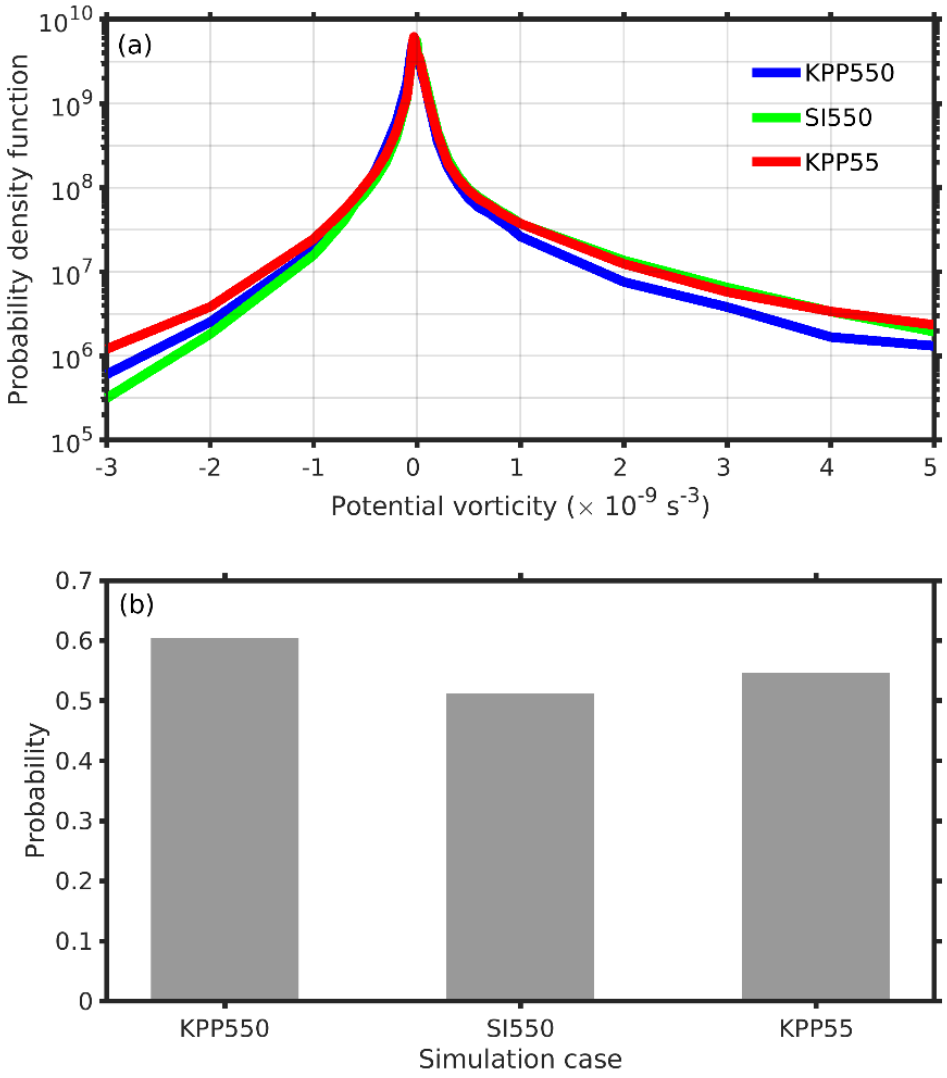

Figure 13 (a) Probability density functions of PV and (b) the probabilities of negative PV in the upper 30 m over NFront at the last day of the simulation in different cases.

3.4 Tracer redistribution

The impacts on tracer redistribution by SI diffusivity are assessed by releasing two types of tracers in these three cases. The tracer fields are homogeneous in horizontal but vary in vertical following a hyperbolic tangent function. The concentration of the first type, C0 has a decreasing trend with depth, namely,

$$C0 = \frac{1}{2}\left(1 - \tanh\left(\frac{z+30}{5}\right)\right). \quad (21)$$

C0 represents tracers that are scarce near the surface but abundant in deep (e.g., nutrients). In contrast, the concentration of the second type, C1 represents tracers that are abundant near the surface (e.g., CO_2),

$$C1 = \frac{1}{2}\left(1 + \tanh\left(\frac{z+30}{5}\right)\right). \quad (22)$$

No surface exchanges are applied for these tracers. Both tracers are released at 12 days and simulated for 5 days.

The tracer concentrations averaged over NFront are shown in Figure 14. The tracer gradients with initial depths around 30 m deepen toward the pycnocline as time evolves in all three cases. The concentration of C0 at the surface increases with time due to the vertical tracer flux (Figure 14a, c, e), while that of C1 at the surface decreases with time (Figure 14b, d, f). Overall, the evolution of the tracers shows similar patterns. The final profiles of the tracers averaged over NFront indicates the differences between the three cases (Figure 15). Compared with KPP550, SI550 reproduces the tracer profiles closer to the high-resolution case KPP55. The differences reach as much as 0.07 between SI550 and KPP550, and 0.05 between KPP55 and KPP550. The most notable differences mainly occur between 20 m and 60 m, emphasizing the importance of SI on exchanges between the SML and ocean interior. It should be noted that the impacts of SI on the tracer redistribution highly depends on the averaging region, initial vertical tracer profiles and SI activity. Nevertheless, the results here highlight that SI and the SI scheme affect tracer redistribution, particularly near the ML base.

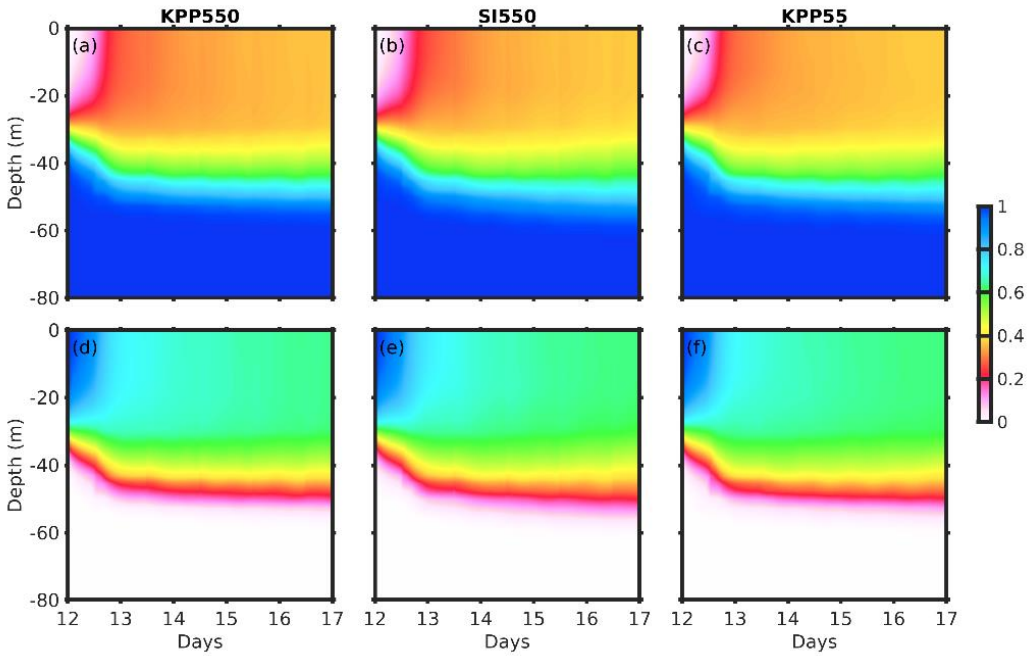

Figure 14 Time evolution of the tracer concentration profiles averaged over NFront in (a, d) KPP550, (b, e) SI550 and (c, f) KPP55.

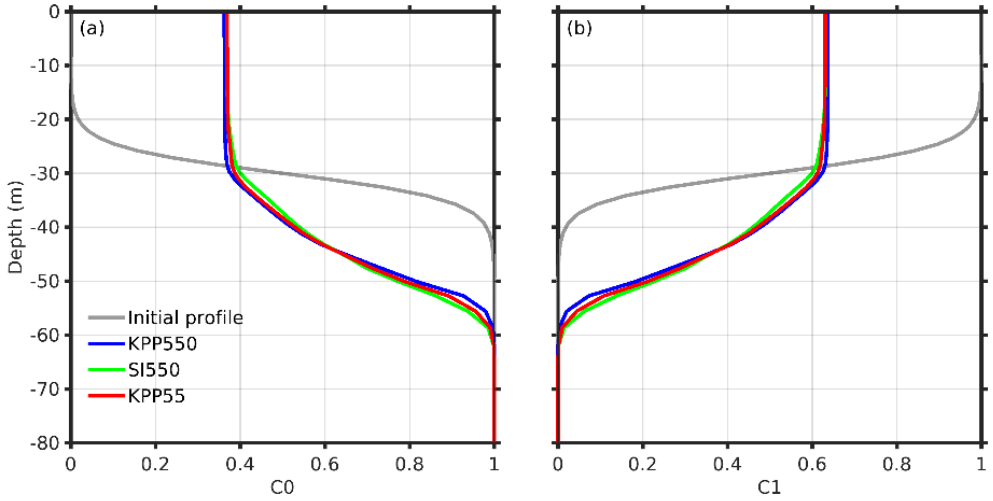

Figure 15 Tracer profiles of (a) C0 and (b) C1 averaged over NFront at the end of 16 days in different cases. The gray lines denote the initial profiles released at 12 days.

4 Discussion and Conclusions

Based on the analysis above, the SI scheme parameterizes the impacts of SI in a SI-unresolved model in many regards. Despite of the good consistency between the coarse-resolution case SI550 and the high-resolution case KPP55, several limitations remain. First of all, the SI scheme applied here is engaged only when both B_0 and *EFB* are positive—i.e., *forced* SI. However, the cross-front velocity perturbations in Figure 4 indicate that SI occurs at the front

even when B_0 is negative. As the control case to directly resolve SI, the high-resolution case is also limited in capturing the full SI effects.

4.1 SI resolving and nonhydrostatic effect

Based on the estimation in Section 2, the initial temperature field allows that the fastest SI growing modes have spatial wavelengths between 0.5 ~ 1.5 km. It can be inferred that the SI scales vary as the front evolves. Based on the output variables from KPP55, the SI wavelengths are estimated based on Equation (2). Here, U and Ri_b are calculated based on the model outputs. Theoretically Ri_b is between $0.25 \leqslant Ri_b \leqslant 0.95$ for SI dominance, so here Ri_b is an average in the SI layer and arbitrarily assigned to be $Ri_b=0.25$ when $Ri_b<0.25$ and $Ri_b=0.95$ when $Ri_b>0.95$. Given that the upper limit wavelength of dynamic processes for a model to resolve is two times of the grid spacings (a requirement from the Nyquist sampling rate), SI that resolved by KPP55 should have wavelengths larger than 110 m. Based on this threshold value, the percentage of the resolved SI in KPP55 is estimated (Figure 16a). Here, the resolved-SI percentage is defined as the percentage of grid points with SI wavelengths larger than 110 m over the total grid points with $h < 0.95H$. According to the estimation, the resolved-SI percentage reaches 70% at the beginning and decrease to about 40% at the end of the simulation. Bachman & Taylor (2014) show that the SI growth curve typically extends about a factor of 2−3 smaller than the peak growth rate, and they argue that these smaller scales are needed for quantitative although not qualitative accuracy.

The small SI spatial scales may also potentially invalidate the hydrostatic approximation used here. To measure this potential nonhydrostatic impact, the hydrostatic parameter of the resolved SI is calculated as (Marshall et al., 1997; Bachman & Taylor, 2014),

$$\eta = \frac{\delta^2}{Ri_b}, \tag{23}$$

where $\delta = H/L_{SI}$ is the aspect ratio, H is the SI layer determined by Equation (3) that can be taken as the vertical scale of SI, and L_{SI} is the SI wavelength determined by Equation (2). The hydrostatic approximation is appropriate and the nonhydrostatic impact is negligible when $\eta \ll 1$.

The hydrostatic parameter at different percentiles and days are shown in Figure 16b. It can be observed that the resolved SI has hydrostatic parameter values up to 0.5, indicating that the nonhydrostatic impact may become important for the smallest SI. However, 85% ~ 95% of the SI as resolved during the simulation period has hydrostatic parameter values less than 0.1 (black line in Figure 16b). The nonhydrostatic effect is believed to be limited for this case here.

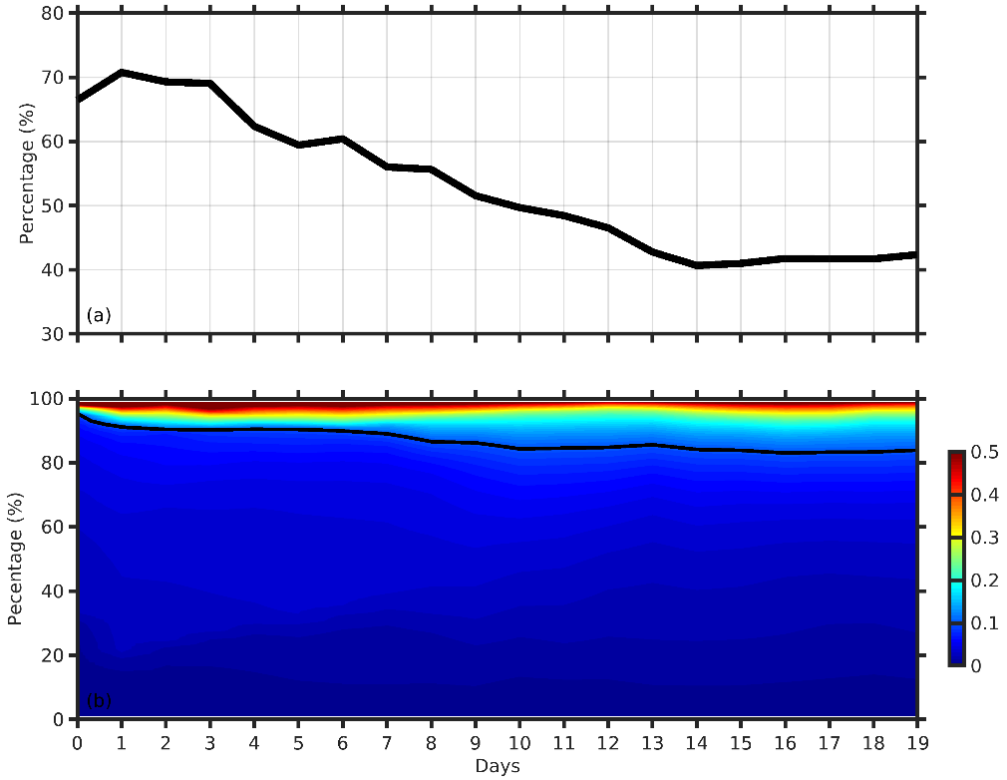

Figure 16 (a) The estimated percentage (%) of the resolved SI and (b) the hydrostatic parameter η distribution in KPP55 during the simulation period. The black line in (b) shows the isoline of η=0.1.

4.2 Prandtl number relation

According to B17, the Prandtl number, *Pr* is an important parameter to link the SI diffusivity and viscosity, which can be evaluated as,

$$Pr = \frac{\upsilon_{SI}}{\kappa_{SI}} = \frac{-\upsilon_{SI} w_{SI} \left(\frac{\partial v_g}{\partial z}\right)^{-1}}{-w_{SI} b_{SI} \left(\frac{\partial b_b}{\partial z}\right)^{-1}}. \quad (24)$$

In the SI scheme, the relation of *Pr* used follows the expression suggested by Anderson (2009),

$$Pr = \frac{1+(10Ri_b)^{0.8}}{2}. \quad (25)$$

Based on the KPP55 results, the calculated *Pr* in the SI-dominated layer (the same depth range with B17, $-1.2h>z>-H$) can be compared to this relation. Similar to the results calculated from LES results in B17, the calculated *Pr* values are scattered in $0 \leqslant Ri_b \leqslant 1$. Following the work by B17, the median, 20th and 80th percentile values in each Ri_b bin (a bin size of 0.1) are calculated and shown (solid line with error bars in Figure 17). Compared with the suggested *Pr* relation, the median *Pr* calculated from KPP55 almost follows the empirical relation at low Ri_b, but generally becomes smaller. The partially SI resolving and hydrostatic approximation may exert impacts on the *Pr* estimate. However, doubts may also exist in the robustness of the empirical relation to describe the relation between SI viscosity and diffusivity. The *Pr* relation is beyond the scope of

this work, and likely requires a nonhydrostatic model to examine, but further work is definitely needed to improve the SI scheme.

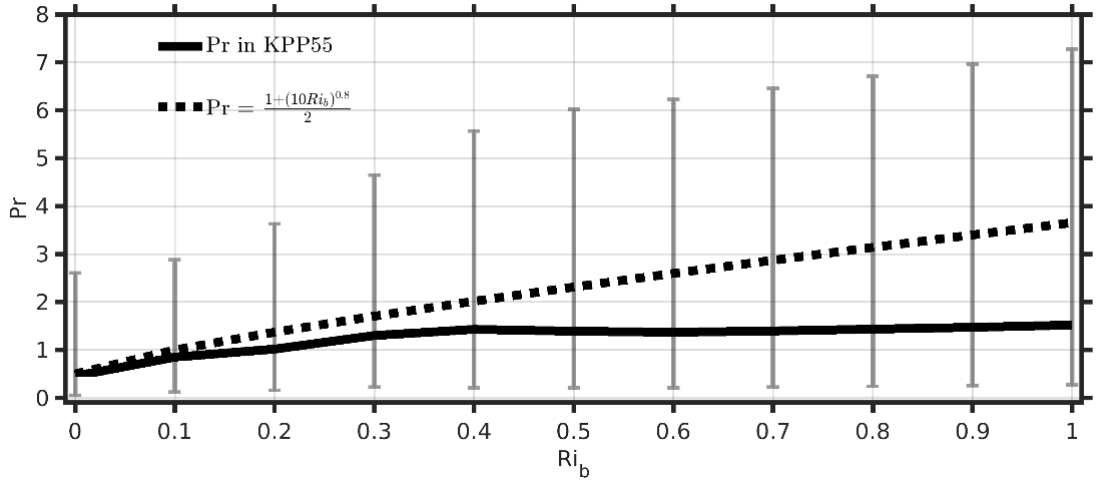

Figure 17 The median *Pr* versus Ri_b in KPP55 (solid line). The error bars denote the 20th and 80th percentile *Pr* values. The dash line denotes the empirical relation between *Pr* and Ri_b in Equation (25).

4.3 Conclusions

The SI scheme proposed by B17 is applied alongside the KPP scheme in the CROCO in this work, and the analysis based on the idealized model simulations indicates positive improvements of the simulation results by the SI scheme.

The GSP is the dominant energy source for SI, and the calculated GSP is remarkably enhanced in these simulations as the model resolution becomes fine enough to resolve SI (KPP55 vs. KPP550). The results from SI550 indicates that the SI scheme improves the GSP magnitude more closely matching the high-resolution case KPP55. In addition to the GSP, the vertical heat fluxes BF (turbulent) and BP (submesoscale) are also modulated by SI. These impacts are also captured by the SI scheme.

Overall, the SML by SI impacts, which is both a direct SI impact and an indirect SI impact through modulating MLI and BP. A primary role of SI is to reduce negative PV. Here SI shifts the median PV closer to a neutral state of PV=0. In order for SI to reduce negative PV, the positive PV becomes more likely in the SI-resolved and SI-parameterized runs than the SI-neglected KPP550 run. Moreover, passive tracers indicate potential contributions of SI on exchanges between the SML and ocean interior.

These simulations indicate the significant effects of the SI scheme in a coarse-resolution model, but the quantitative values in this work are based on idealized model simulations with an idealized front. To measure SI contributions in the real oceans, a more realistic model with and without the SI scheme included must be compared.

Acknowledgements. This work is supported by the National Key Research and Development Program of China (2017YFA0604100). JHD acknowledges support from and the National Natural Science Foundation of China (41806025) and the China Scholarship Council. BFK acknowledges support from NSF OCE-1350795. CMD appreciates the support from the National Key Research and Development Program of China (2016YFA0601803), the National Natural Science Foundation of China (41476022, 41490643), the National Programme on Global Change and Air-Sea Interaction (GASI-03-IPOVAI-05), and the foundation of China Ocean Mineral Resources R & D Association (DY135-E2-2-02, DY135-E2-3-01). The code of the SI scheme and model configurations are available at https://github.com/jhdong2016/SI_model. The data for analysis and setting up the simulations available at https://doi.org/10.5281/zenodo.3988614.

References

Anderson, P. S. (2009). Measurement of Prandtl number as a function of Richardson number avoiding self-correlation. *Boundary-layer meteorology*, *131*(3), 345-362. doi:10.1007/s10546-009-9376-4

Bachman, S. D., & Taylor, J. R. (2014). Modelling of partially-resolved oceanic symmetric instability. *Ocean Modelling*, *82*, 15-27. doi:10.1016/j.ocemod.2014.07.006

Bachman, S. D., Fox-Kemper, B., Taylor, J. R., & Thomas, L. N. (2017). Parameterization of frontal symmetric instabilities. I: Theory for resolved fronts. *Ocean Modelling*, *109*, 72-95. doi:10.1016/j.ocemod.2016.12.003

Boccaletti, G., Ferrari, R., & Fox-Kemper, B. (2007). Mixed layer instabilities and restratification. *Journal of Physical Oceanography*, *37*(9), 2228-2250. doi:10.1175/JPO3101.1

Bodner, A., & Fox-Kemper. B. (2020) A breakdown in potential vorticity estimation delineates the submesoscale-to-turbulence boundary in large eddy simulations. *Journal of Advances in Modeling Earth Systems*, *12*, e2020MS002049. doi:10.1029/2020MS002049

Buckingham, C. E., Lucas, N., Belcher, S., Rippeth, T., Grant, A., Le Sommer, J., . . . Garabato, A. C. N. (2019). The contribution of surface and submesoscale processes to turbulence in the open ocean surface boundary layer. *Journal of Advances in Modeling Earth Systems*, 11(12), 4066-4094. doi:10.1029/2019MS001801

Buckingham, C. E., Naveira Garabato, A. C., Thompson, A. F., Brannigan, L., Lazar, A., Marshall, D. P., . . . Belcher, S. E. (2016). Seasonality of submesoscale flows in the ocean surface boundary layer. *Geophysical Research Letters*, *43*(5), 2118-2126. doi:10.1002/2016GL068009

Callies, J., Ferrari, R., Klymak, J. M., & Gula, J. (2015). Seasonality in submesoscale turbulence. *Nature Communications*, *6*, 6862. doi:10.1038/ncomms7862

Capet, X., McWilliams, J. C., Molemaker, M. J., & Shchepetkin, A. (2008a). Mesoscale to submesoscale transition in the California Current System. Part III: Energy balance and flux. *Journal of Physical Oceanography*, *38*(10), 2256-2269. doi:10.1175/2008JPO3810.1

Capet, X., McWilliams, J. C., Molemaker, M. J., & Shchepetkin, A. F. (2008b). Mesoscale to submesoscale transition in the California Current System. Part I: Flow structure, eddy flux, and

observational tests. *Journal of Physical Oceanography*, *38*(1), 29-43. doi: 10.1175/2007JPO3671.1

D'Asaro, E., Lee, C., Rainville, L., Harcourt, R., & Thomas, L. (2011). Enhanced turbulence and energy dissipation at ocean fronts. *Science, 332*(6027), 318-322. doi:10.1126/science.1201515

de Boyer Montégut, C., Madec, G., Fischer, A. S., Lazar, A., & Iudicone, D. (2004). Mixed layer depth over the global ocean: An examination of profile data and a profile-based climatology. *Journal of Geophysical Research: Oceans*, *109*(C12). doi:10.1029/2004JC002378

de Marez, C., Carton, X., Corréard, S., L'Hégaret, P., & Morvan, M. (2020). Observations of a deep submesoscale cyclonic vortex in the Arabian Sea. *Geophysical Research Letters*, *47*(13), e2020GL087881. doi:10.1029/2020GL087881

Dong, J., Fox-Kemper, B., Zhang, H., & Dong, C. (2020a). The seasonality of submesoscale energy production, content, and cascade. *Geophysical Research Letters*, e2020GL087388. doi:10.1029/2020GL087388

Dong, J., Fox-Kemper, B., Zhang, H., & Dong, C. (2020b). The scale and activity of symmetric instability globally. *Journal of Physical Oceanography*, under review. http://www.geo.brown.edu/research/Fox-Kemper/pubs/pdfs/DongFox-Kemper20b.pdf

Fox-Kemper, B., Danabasoglu, G., Ferrari, R., Griffies, S. M., Hallberg, R. W., Holland, M. M., . . . Samuels, B. L. (2011). Parameterization of mixed layer eddies. III: Implementation and impact in global ocean climate simulations. *Ocean Modelling*, *39*(1-2), 61-78. doi:10.1016/j.ocemod.2010.09.002

Fox-Kemper, B., Ferrari, R., & Hallberg, R. (2008). Parameterization of mixed layer eddies. Part I: Theory and diagnosis. *Journal of Physical Oceanography*, *38*(6), 1145-1165. doi:10.1175/2007JPO3792.1

Grant, A.L. and Belcher, S.E., 2009. Characteristics of Langmuir turbulence in the ocean mixed layer. *Journal of Physical Oceanography*, *39*(8), pp.1871-1887. doi:10.1175/2009JPO4119.1

Gula, J., Molemaker, M. J., & McWilliams, J. C. (2016). Topographic generation of submesoscale centrifugal instability and energy dissipation. *Nature Communications*, *7*, 12811. doi:10.1038/ncomms12811

Haine, T. W., & Marshall, J. (1998). Gravitational, symmetric, and baroclinic instability of the ocean mixed layer. *Journal of Physical Oceanography*, *28*(4), 634-658. doi:10.1175/1520-0485(1998)028<0634:GSABIO>2.0.CO;2

Hamlington, P. E., Van Roekel, L. P., Fox-Kemper, B., Julien, K., & Chini, G. P. (2014). Langmuir–submesoscale interactions: Descriptive analysis of multiscale frontal spindown simulations. *Journal of Physical Oceanography*, *44*(9), 2249-2272. doi:10.1175/JPO-D-13-0139.1

Haney, S., Fox-Kemper, B., Julien, K., & Webb, A. (2015). Symmetric and geostrophic instabilities in the wave-forced ocean mixed layer. *Journal of Physical Oceanography*, *45*(12), 3033-3056. doi:10.1175/JPO-D-15-0044.1

Hedström, K., (2009). Technical Manual for a Coupled Sea-Ice/Ocean Circulation Model (Version 3). U.S. Department of the Interior Minerals Management Service Anchorage, Alaska (2009) Contract No. M07PC13368.

Hoskins, B. (1974). The role of potential vorticity in symmetric stability and instability. *Quarterly Journal of the Royal Meteorological Society*, *100*(425), 480-482. doi:10.1002/qj.49710042520

Jullien, S., Caillaud, M., Benshila, R., Bordois, L., Cambon, G., Dumas, F., Le Gentil, S., Lemarié, F., Marchesiello, P., & Theetten, S. (2019). Technical and numerical doc. https://www.croco-ocean.org/documentation/

Large, W. G., McWilliams, J. C., & Doney, S. C. (1994). Oceanic vertical mixing: A review and a model with a nonlocal boundary layer parameterization. *Reviews of Geophysics*, *32*(4), 363-403. doi:10.1029/94RG01872

Lévy, M., Ferrari, R., Franks, P. J., Martin, A. P., & Rivière, P. (2012). Bringing physics to life at the submesoscale. *Geophysical Research Letters*, *39*(14). doi:10.1029/2012GL052756. doi:10.1029/2012GL052756

Li, Q., Webb, A., Fox-Kemper, B., Craig, A., Danabasoglu, G., Large, W. G., & Vertenstein, M. (2016). Langmuir mixing effects on global climate: WAVEWATCH III in CESM. *Ocean Modelling*, *103*, 145-160. doi:10.1016/j.ocemod.2015.07.020

Li, Q. and Fox-Kemper, B., 2017. Assessing the effects of Langmuir turbulence on the entrainment buoyancy flux in the ocean surface boundary layer. *Journal of Physical Oceanography*, *47*(12), pp.2863-2886. doi:10.1175/JPO-D-17-0085.1

Li, Q. and Fox-Kemper, B., 2020. Anisotropy of Langmuir turbulence and the Langmuir-enhanced mixed layer entrainment. *Physical Review Fluids*, *5*(1), p.013803. doi:10.1103/PhysRevFluids.5.013803

Marshall, J., Hill, C., Perelman, L., & Adcroft, A. (1997). Hydrostatic, quasi-hydrostatic, and nonhydrostatic ocean modeling. *Journal of Geophysical Research: Oceans*, *102*(C3), 5733-5752. doi:10.1029/96JC02776

McWilliams, J. C. (2016). Submesoscale currents in the ocean. *Proceedings of the Royal Society A*, *472*(2189), 20160117. doi:10.1098/rspa.2016.0117

Molemaker, M. J., McWilliams, J. C., & Dewar, W. K. (2015). Submesoscale instability and generation of mesoscale anticyclones near a separation of the California Undercurrent. *Journal of Physical Oceanography*, *45*(3), 613-629. doi:10.1175/JPO-D-13-0225.1

Noh, Y., Ok, H., Lee, E., Toyoda, T., & Hirose, N. (2016). Parameterization of Langmuir circulation in the ocean mixed layer model using LES and its application to the OGCM. *Journal of Physical Oceanography*, *46*(1), 57-78. doi:10.1175/JPO-D-14-0137.1

Qiao, F., Yuan, Y., Deng, J., Dai, D., & Song, Z. (2016). Wave–turbulence interaction-induced vertical mixing and its effects in ocean and climate models. *Philosophical Transactions of the Royal Society A: Mathematical, Physical and Engineering Sciences*, *374*(2065), 20150201. doi:10.1098/rsta.2015.0201

Redi, M. H. (1982). Oceanic isopycnal mixing by coordinate rotation. *Journal of Physical Oceanography*, *12*(10), 1154-1158. doi:10.1175/1520-0485(1982)012<1154:OIMBCR>2.0.CO;2

Siegelman, L., Klein, P., Rivière, P., Thompson, A. F., Torres, H. S., Flexas, M., & Menemenlis, D. (2019). Enhanced upward heat transport at deep submesoscale ocean fronts. *Nature Geoscience*, 1-6. doi:10.1038/s41561-019-0489-1

Smith, K. M., Hamlington, P. E., & Fox-Kemper, B. (2016). Effects of submesoscale turbulence on ocean tracers. *Journal of Geophysical Research: Oceans*, *121*(1), 908-933. doi:10.1002/2015JC011089

Stone, P. H. (1966). On non-geostrophic baroclinic stability. *Journal of the atmospheric sciences*, *23*(4), 390-400. doi:10.1175/1520-0469(1966)023<0390:ONGBS>2.0.CO;2

Su, Z., Wang, J., Klein, P., Thompson, A. F., & Menemenlis, D. (2018). Ocean submesoscales as a key component of the global heat budget. *Nature Communications*, *9*(1), 775. doi:10.1038/s41467-018-02983-w

Taylor, J. R., & Ferrari, R. (2010). Buoyancy and wind-driven convection at mixed layer density fronts. *Journal of Physical Oceanography*, *40*(6), 1222-1242. doi:10.1175/2010JPO4365.1

Thomas, L. N. (2005). Destruction of potential vorticity by winds. *Journal of Physical Oceanography*, *35*(12), 2457-2466. doi:10.1175/JPO2830.1

Thomas, L. N., Tandon, A., & Mahadevan, A. (2008). Submesoscale processes and dynamics. *Ocean modeling in an Eddying Regime*, 17-38. doi:10.1029/177GM04. doi:10.1029/177GM04

Thomas, L. N., Taylor, J. R., Ferrari, R., & Joyce, T. M. (2013). Symmetric instability in the Gulf Stream. *Deep Sea Research Part II: Topical Studies in Oceanography*, *91*, 96-110. doi:10.1016/j.dsr2.2013.02.025

Thompson, A. F., Lazar, A., Buckingham, C., Naveira Garabato, A. C., Damerell, G. M., & Heywood, K. J. (2016). Open-ocean submesoscale motions: A full seasonal cycle of mixed layer instabilities from gliders. *Journal of Physical Oceanography*, *46*(4), 1285-1307. doi:10.1175/JPO-D-15-0170.1

Wenegrat, J. O., Thomas, L. N., Sundermeyer, M. A., Taylor, J. R., D'Asaro, E. A., Klymak, J. M., . . . Lee, C. M. (2020). Enhanced mixing across the gyre boundary at the Gulf Stream front. *Proceedings of the National Academy of Sciences*. doi:10.1073/pnas.2005558117

Yu, X., Naveira Garabato, A. C., Martin, A. P., Buckingham, C. E., Brannigan, L., & Su, Z. (2019). An annual cycle of submesoscale vertical flow and restratification in the upper ocean. *Journal of Physical Oceanography*, *49*(6), 1439-1461. doi:10.1175/JPO-D-18-0253.1

Zhu, J. (2017). Descriptive analysis of frontal symmetric instabilities without background temperature gradient. *Brown University*. http://www.geo.brown.edu/research/Fox-Kemper/pubs/pdfs/Zhu17.pdf